A NOVEL TWO-WAY COUPLING METHOD FOR THE STUDY OF THE AEROELASTICITY OF WIND TURBINES IN A LARGE-EDDY SIMULATION FRAMEWORK

G. Della Posta[1] - U. Ciri[2] - S. Leonardi[2] - M. Bernardini[1]

[1] Dept. of Aerospace and Mechanical Engr., Sapienza University of Rome, Rome, RM, 00184, Italy (giacomo.dellaposta@uniroma1.it, matteo.bernardini@uniroma1.it)
[2] Dept. of Mechanical Engr., University of Texas at Dallas, Richardson, TX, 75080, USA (umberto.ciri@utdallas.edu, stefano.leonardi@utdallas.edu)

ABSTRACT

The constant up-scaling of wind turbines encourages researchers to develop innovative aeroelastic models for the study of Fluid-Structure Interaction in wind energy. In this paper, we present a novel two-way coupling method joining a Large-Eddy Simulation fluid solver and a modal beam-like structural solver. The model takes advantage of the Actuator Line Model representing the rotor in the fluid domain, and exploits the superior accuracy of the high-fidelity Computational Fluid Dynamics solver to describe the complex aerodynamics of wind turbines. The comparison for a benchamark turbine between the cases with and without aeroelastic feedback showed how significantly the coupling procedure affects the structural dynamics, especially when the blades pass in front of the tower. Conversely, the coupled fluid field was only slightly altered in the proximity of the turbine. Moreover, the considerable magnitude of the rotational deformations suggest their potential importance in future developments.

KEYWORDS

Aeroelasticity; Large Eddy Simulation; Modal Structural Dynamics; Actuator Line Model

NOMENCLATURE

C_d, C_l	lift and drag coefficients	FoR	frame of reference
C_m	aerodynamic moment coefficient	$\boldsymbol{f}^{aero}$	aerodynamic force vector
C_p, C_t	power and thrust coefficients	F_d, F_l	drag and lift forces per unit length
C_s	Smagorinsky constant	$\boldsymbol{f}^{\boldsymbol{t}}$	body force from rotor model
C_t	Thrust coefficient	$\mathbf{K}$	modal structural stiffness matrix
c	airfoil chord	$\mathbf{K^c}$	modal centrifugal stiffness matrix
D	turbine diameter	$\mathbf{K^E}$	modal Euler stiffness matrix
$\mathbf{D}$	modal structural damping matrix	k_{gen}	control gain of the turbine
$\mathbf{D^C}$	modal Coriolis damping matrix	I	rotational inertia of the rotor
$\boldsymbol{d}$	displacement vector in relative FoR	$\mathbf{I}$	identity matrix
d_i	displacement along $\boldsymbol{E}_i$	L	length of the blade
$\boldsymbol{E}_i$	i-th versor of the rotating FoR	M	number of structural modes
$\boldsymbol{e}$	modal external load array	$\mathbf{M}$	modal structural mass matrix
$\boldsymbol{e}^c$	modal centrifugal load array	M^{aero}	aerodynamic moment
$\boldsymbol{e}^E$	modal Euler load array	N	number of structural nodes
F	Prandtl correction factor	P	filtered pressure
f_i	i-th structural natural frequency	$\hat{P}$	modified pressure

Q	2nd invariant of vel. gradient	Θ	azimuthal angle of the blade
$\boldsymbol{q}$	modal coordinates array	θ_i	angular displ. around $\boldsymbol{E}_i$
r	radial position along the blade	λ	tip speed ratio
R	radius of the rotor	ν	air kinematic viscosity
R_h	radius of the hub	ν_{sgs}	subgrid eddy viscosity
$\boldsymbol{R}_{OP}$	position vector in undeformed conf.	ρ	air density
Re	Reynolds number	ρ_s	structure density
$\bar{\boldsymbol{S}}$	filtered strain rate tensor	$\boldsymbol{\tau}$	sub-grid scale (SGS) tensor
T_{aero}	external aerodynamic torque	$\boldsymbol{\tau}^{\boldsymbol{d}}$	deviatoric part of the SGS tensor
T_{gen}	generator torque	ϕ	twist angle
t	time	$\boldsymbol{\psi}^m$	m-th elastic mode shape
$\boldsymbol{U}$	filtered velocity vector	Ω	rotor angular speed
$\boldsymbol{U_{rel}}$	relative velocity vector	ω_i	angular deform. vel. around $\boldsymbol{E}_i$
U_∞	undisturbed reference velocity	$\cdot$	scalar product
$\mathcal{V}$	structural volume	$\times$	vector product
$\boldsymbol{v}$	struct. deformation velocity vec.	$\otimes$	tensor product
v_i	deform. velocity along $\boldsymbol{E}_i$	$\dot{(\bullet)}, \ddot{(\bullet)}$	time derivation
$\boldsymbol{X}$	coord. vector in the rotating FoR	sym	symmetric operator
$\boldsymbol{x}$	coord. vector in the fixed FoR	tr	trace operator
α	angle of attack	$\bar{a}, A$	filtered part of variable a
Δ	sub-grid scale filter width	$\tilde{a}$	time avg of variable a
Δx_i	grid spacing in i-th fixed direction	$\langle a \rangle$	azimuthal phase avg of variable a
ϵ	actuator line spreading radius		

INTRODUCTION

The increased demand for clean electricity of the last decades has encouraged the development of renewable energy science and in particular of wind energy, because of its technological maturity and economical competitiveness (Komusanac et al., 2019).

To maximise the power capture and minimise the costs, the size of wind turbines has been constantly increasing, making them the largest rotating machines on Earth. However, rotor diameters exceding 200 m entail major modifications on the structure, in particular on the long and slender blades, whose increasing flexibility will lead to a more intense Fluid-Structure Interaction (FSI). For this reason, researchers advocate new advanced models for the study of aeroelasticity that are capable of capturing the different spatial and temporal scales involved in this problem (Van Kuik et al., 2016).

Today's aeroelastic models, such as FAST (Jonkman and Buhl Jr, 2005) and HAWC2 (Larsen and Hansen, 2007), are mainly based on low-fidelity aerodynamics models, such as the Blade Element Momentum (BEM) theory. However, despite the high numerical efficiency, researchers have found that the simplifying assumptions of BEM theory may cause revelant errors in the modelling of the complex unsteady 3D aerodynamics, even if correction models are included (Simms et al., 2001).

Because of the paucity of experimental studies on utility-scale wind turbines, high-fidelity numerical models will be crucial for the turbine design process. Recently, researchers have thus tried to leverage the superior accuracy of Computational Fluid Dynamics (CFD) and Computational Structural Dynamics (CSD) to better characterise the complex aerodynamics and the mutual interaction between fluid and structure for big wind turbines.

One of the first CFD-CSD studies of the 3D FSI of the full machine, including tower and

nacelle, was reported in Hsu and Bazilevs (2012). The authors coupled a low-order Finite Element Method (FEM) to model the aerodynamics (ALE-VMS technique) with an Isogeometric Analysis (IGA) to model the structural dynamics. The results have shown an important impact of the tower shadowing and a non-symmetric blade deformation. In Churchfield et al. (2012), the National Renewable Energy Laboratory (NREL) presented the aeroelastic tool SOWFA (Simulator for Off/Onshore Wind Farm Applications), in which they coupled the OpenFOAM Large-Eddy Simulation (LES) solver for the fluid dynamics with the FAST module, which combines modal and multibody representations for the structural dynamics of the entire turbine. To represent the action of the blades in the fluid domain avoiding expensive body-fitted meshes, the authors used a Generalised Actuator Disc model: the Actuator Line Model (ALM) proposed by Sorensen and Shen (2002). Heinz (2013) linked the multibody structural solver of HAWC2 with a 3D Reynolds Averaged Navier-Stokes Equations (RANS) solver. The comparison between the simulations with loose and strong couplings showed that for the study of FSI of wind turbines, exchanging information between the solvers only once per time step (*loose coupling*) is sufficient to provide accurate results. Recently, Meng et al. (2018) proposed the Elastic Actuator Line Model (EALM), a two-way coupling method which combines a RANS approach, employing the actuator line modelling, with a finite difference structural solver based on a rotating cantilever Euler-Bernoulli beam with only flexural behaviour.

This work presents a novel high-fidelity CFD-CSD model for the aeroelastic study of wind turbines. The method couples in a loosely manner our in-house LES fluid solver, in which the rotor is modelled by means of the Actuator Line Model, to a modal structural solver, which considers only the blades represented as cantilever rotating equivalent 1D beams. In this initial study, the fluid solver evaluates the aerodynamic loads at each section of the blades by defining the local effective incidence as a function of the fluid velocity field and of the instantaneous deformation velocity of the structure. The blades' motion, in turn, is forced by the instantaneous loading provided by the fluid solver. The tower and the nacelle are modelled in the fluid domain by means of an Immersed Boundary Method (IBM) (Orlandi and Leonardi, 2006).
In our study, we considered the reference onshore 5 MW wind turbine defined by the NREL (Jonkman et al., 2009). We compared the results of the simulations with a rigid structure with those with a flexible structure, by examining power and thrust coefficients, structural deformations and fluid quantities. We found that the coupling has a relevant effect on the aerodynamic loading, especially because of the tower shadowing effect on the structural dynamics. Moreover, coupled simulations allowed us to confirm previous findings regarding the larger aerodynamic damping of the flapwise (out-of-plane) motion of the blade compared to the edgewise (in-plane) one (Hansen, 2007). On the other hand, we observed how fluid quantities are relatively insensitive to this kind of coupling by means of the induced-vibration velocities.

The paper is organised as follows: in the next section, we will present the methodology of the fluid and structural solvers and their coupling; then, after reporting the simulation setup used, we will illustrate the results of the comparison between the rigid and the flexible cases; in the end, we will summarise the main conclusions of our study and its future improvements.

METHODOLOGY

In this section, we present the fluid and structural solvers and the coupling approach used.

The fluid solver

To model the fluid domain, we chose the LES approach. In fact, because of the large separation of scales for the big wind energy problem, Direct Numerical Simulation (DNS) of the Navier-Stokes at real Reynolds numbers are unfeasible even for modern supercomputers. RANS simulations would reduce the expense, but turbulence modelling is afflicted with known problems in the description of separated regions and of unsteady flows. The Large-Eddy Simulation approach, instead, allows researchers to model unsteady turbulent flows with superior accuracy compared to RANS, but with affordable computational resources compared to DNS.

The governing equations of our LES solver (Santoni et al., 2017) are the filtered incompressible Navier-Stokes equations:

$$\nabla \cdot \boldsymbol{U} = 0\,, \tag{1}$$

$$\frac{\partial \boldsymbol{U}}{\partial t} + \nabla \cdot (\boldsymbol{U} \otimes \boldsymbol{U}) = -\nabla \hat{P} + \frac{1}{Re}\nabla^2 \boldsymbol{U} - \nabla \cdot \boldsymbol{\tau}^d + \boldsymbol{f^t}\,, \tag{2}$$

where $\boldsymbol{U}$ is the filtered velocity vector field; $\hat{P}$ is the modified pressure, sum of the filtered pressure P and of the isotropic part of the Sub-Grid Scale (SGS) tensor $\boldsymbol{\tau} = \overline{\boldsymbol{u} \otimes \boldsymbol{u}} - \boldsymbol{U} \otimes \boldsymbol{U} = \boldsymbol{\tau}^d + \frac{1}{3}\mathrm{tr}(\tau)\mathbf{I}$; Re is the Reynolds number based on the turbine's diameter D, the undisturbed inflow velocity U_∞ and the air kinematic viscosity ν; $\boldsymbol{f^t}$ are the body forces of the rotor model. To represent the SGS tensor, we adopted the Boussinesq's hypothesis, and we used the Smagorinsky model to express the subgrid eddy viscosity ν_{sgs} as a function of the filtered strain rate tensor $\bar{\mathbf{S}}$ and the filter width $\Delta = (\Delta x_1 \Delta x_2 \Delta x_3)^{1/3}$, provided by the grid spacing Δx_i. According to our previous works (Santoni et al., 2017), we chose a Smagorinsky constant equal to $C_s = 0.09$. A finite-difference method discretises the governing equations on an orthogonal staggered grid. Second-order central schemes approximate derivatives in space. Time advancement is carried out by a hybrid third-order low-storage Runge-Kutta (RK) scheme treating implicitly the linear terms and explicitly the non-linear terms of the equations. Finally, a fractional step method enforces the solenoidal constraint on velocity and updates the pressure accordingly (Orlandi, 2012). The Message Passing Interface (MPI) paradigm parallelises the code.

To represent the action of the blades on the fluid, we adopted the Actuator Line Model (Sorensen and Shen, 2002). According to this method, the blades are represented in the fluid domain as body forces distributed along radial lines rotating with the rotor angular speed. The local aerodynamic forces are determined by a blade element approach using the tabulated airfoil data and the velocity field determined by the fluid solver at each section of the blades. The body forces are finally obtained by spreading the aerodynamic forces around the actuator lines by means of a kernel function, to avoid numerical instabilities.

For a 2D airfoil, the lift and the drag forces per unit length are respectively:

$$F_l = \frac{1}{2}\rho U_{rel}^2 c C_l(\alpha) F \qquad \text{and} \qquad F_d = \frac{1}{2}\rho U_{rel}^2 c C_d(\alpha) F\,, \tag{3}$$

where ρ is the air density, U_{rel} is the local relative velocity, c is the chord length of the airfoil, $C_l(\alpha)$ and $C_d(\alpha)$ are the lift and drag coefficients at the local angle of attack α. To consider 3D effects on the 2D airfoil data and to limit the overprediction of the aerodynamic loads at the blade hub and tip, we used a modified Prandtl correction factor F (Shen et al., 2005):

$$F = \frac{4}{\pi^2}\cos^{-1}\left[\exp\left(-g\frac{3}{2}\frac{R-r}{r\sin(\alpha+\phi)}\right)\right]\cos^{-1}\left[\exp\left(-g\frac{3}{2}\frac{r-R_h}{r\sin(\alpha+\phi)}\right)\right], \tag{4}$$
$$\text{with} \quad g = \exp\left[-0.125\,(3\,\lambda - 21.0)\right] + 0.1\,,$$

where r is the local radial position, R is the rotor radius, R_h is the hub radius, ϕ is the local twist angle , and $\lambda = \Omega R/U_\infty$ is the tip speed ratio, where Ω is the rotor angular speed.

In the end, we obtained the body force in eq.2 by filtering the aerodynamic force vector $\boldsymbol{f^{aero}}$ by means of a 2D Gaussian spreading function:

$$\boldsymbol{f^t} = -\frac{1}{\epsilon^2\pi}\exp\left[-\left(\frac{r_\eta}{\epsilon}\right)^2\right]\boldsymbol{f^{aero}}\,, \tag{5}$$

where r_η is the radial distance of a generic point in the spreading volume from the centre of the actuator line and ϵ is the spreading radius. As suggested in Troldborg et al. (2009), we used a spreading radius $\epsilon = 2\Delta$ to avoid numerical instabilities.

To fully determine the loading conditions on the structure, we also defined similarly the aerodynamic moment referred to the quarter of chord, *i.e.* the centre of the structural axes, as:

$$M^{aero} = -\frac{1}{2}\rho U_{rel}^2 c^2 C_m(\alpha) F\,, \tag{6}$$

with $C_m(\alpha)$ local pitching moment coefficient. The minus accounts for the opposite signs between the nose-up airfoil data convention and our nose-down positive torsion.

We modelled the fixed elements of the turbine, *i.e.* the tower and the nacelle, by means of an IBM procedure already validated in Santoni et al. (2017), and we used a 1D model equation to determine the rotor angular speed:

$$I\dot{\Omega} = T_{aero} - T_{gen} \quad \text{with} \quad T_{gen} = k_{gen}\Omega^2\,, \tag{7}$$

where I is the inertia of the rotor, T_{aero} is the external aerodynamic torque, and T_{gen} is the generator torque. For our variable-speed turbine, we assumed a standard quadratic control law (Laks et al., 2009) with a turbine-dependent torque gain k_{gen}.

The structural solver

Because of their direct impact on the aerodynamics and the significant stiffness of the tower and the shaft, in our structural model we considered only the dynamics of the blades. We modelled the blades as rotating cantilever beams fixed at the rotor's hub, under the assumption of small deformations, by means of a modal structural method. We described the structural dynamics in a relative Frame of Reference (FoR) rotating with the beams.
According to these assumptions, the elastic displacement along the neutral axis of the beam is:

$$\boldsymbol{d}\left(X_1, t\right) = \sum_{m=1}^{M} q_m(t)\,\boldsymbol{\psi}^m\left(X_1\right) \tag{8}$$

where $\boldsymbol{\psi}^m\left(X_1\right)$ is the m-th elastic mode shape along the X_1 coordinate starting from the hub, q_m is the correspondant modal coordinate, and M is the number of modes considered.

The finite element model used for the modal analysis was based on complete 6 DFs beam elements having Euler-Bernoulli behaviour for bending and linear shape functions for the axial and torsional DFs. We assumed a lumped-mass representation properly considering the local offset of the centres of mass, and we used a normal mass normalisation for the definition of the modes. The natural frequencies obtained match the ones of other studies (Jeong et al., 2014).

To include the effects of the motion of the relative FoR in the fixed FoR, we expressed the inertial coupling terms in modal basis according to the approach proposed by Reschke (2005)

and further developed by Saltari et al. (2017). From the principle of the virtual work for a deformable body under a generic motion, we decomposed the absolute acceleration in its relative, centrifugal, Coriolis and Euler contributions. The following system of equations represented the elastic dynamics of each blade in modal basis:

$$\mathbf{M}\,\ddot{\boldsymbol{q}} + \left[\mathbf{D} + \mathbf{D}^{C}\left(\boldsymbol{\Omega}\right)\right]\dot{\boldsymbol{q}} + \left[\mathbf{K} + \mathbf{K}^{c}\left(\boldsymbol{\Omega}\right) + \mathbf{K}^{E}(\dot{\boldsymbol{\Omega}})\right]\boldsymbol{q} = \boldsymbol{e} + \boldsymbol{e}^{c}\left(\boldsymbol{\Omega}\right) + \boldsymbol{e}^{E}(\dot{\boldsymbol{\Omega}}) \tag{9}$$

where $\mathbf{M}$ and $\mathbf{K}$ are the structural mass and stiffness matrices in modal basis, $\boldsymbol{e}$ is the modal external load, made of the instantaneous aerodynamic and gravity forces, and $\mathbf{D}$ is the structural damping matrix, defined by a constant modal damping for all the modes. The other remaining terms are the inertial contributions and are made of:

- the centrifugal stiffness matrix and load

$$\mathrm{K}^{c}_{nm} = \boldsymbol{\Omega}\cdot\mathrm{sym}\left\{\iiint_{\mathcal{V}}\rho_s\left[\left(\boldsymbol{\psi}^{m}\cdot\boldsymbol{\psi}^{n}\right)\mathbf{I} - \boldsymbol{\psi}^{m}\otimes\boldsymbol{\psi}^{n}\right]\,\mathrm{d}V\right\}\boldsymbol{\Omega}\,, \tag{10}$$

$$\mathrm{e}^{c}_{n} = -\boldsymbol{\Omega}\cdot\mathrm{sym}\left\{\iiint_{\mathcal{V}}\rho_s\left[\left(\boldsymbol{R}_{OP}\cdot\boldsymbol{\psi}^{n}\right)\mathbf{I} - \boldsymbol{R}_{OP}\otimes\boldsymbol{\psi}^{n}\right]\,\mathrm{d}V\right\}\boldsymbol{\Omega}\,, \tag{11}$$

- the Coriolis damping matrix

$$\mathrm{D}^{C}_{nm} = 2\,\boldsymbol{\Omega}\cdot\iiint_{\mathcal{V}}\rho_s(\boldsymbol{\psi}^{m}\times\boldsymbol{\psi}^{n})\,\mathrm{d}V\,, \tag{12}$$

- the Euler stiffness matrix and load

$$\mathrm{K}^{E}_{nm} = -\dot{\boldsymbol{\Omega}}\cdot\iiint_{\mathcal{V}}\rho_s(\boldsymbol{\psi}^{m}\times\boldsymbol{\psi}^{n})\,\mathrm{d}V \quad\text{and}\quad \mathrm{e}^{E}_{n} = -\dot{\boldsymbol{\Omega}}\cdot\iiint_{\mathcal{V}}\rho_s(\boldsymbol{R}_{OP}\times\boldsymbol{\psi}^{n})\,\mathrm{d}V\,, \tag{13}$$

where $\boldsymbol{R}_{OP}$ is the vector from the hub centre to the generic point P in the undeformed configuration, $\mathbf{I}$ is the identity matrix, sym extracts the symmetric part of the following matrix, ρ_s is the structural density and $\mathcal{V}$ is the structural volume. We discretised these terms according to the procedure described in Saltari et al. (2017). The second-order accurate generalised-α method (Chung and Hulbert, 1993) integrates in time the structural dynamics.

The coupling method

Our aeroelastic model leverages the formulation of the Actuator Line Model and allowed us to avoid the presence of complex interfaces between the fluid and the structural problems.
Each physical subproblem has its own independent or *staggered* solver exchanging information with the other one only once per time step (*loose* coupling). We chose to implement a Non-Conventional Serial Staggered (NCSS) coupling algorithm (Farhat and Lesoinne, 1996) which allowed us to advance fluid and structural dynamics simultaneously and to restrict inter-field communications only at the beginning of each RK-substep. By means of this method, we thus managed to avoid subcycling between the two solvers, which would have damaged the overall performance of the code. According to the algorithm, to estimate the new fluid and structural states at a certain instant, we evaluated the aerodynamic forces by using the blade's distribution of the angle of attack determined by the fluid velocity field and the structural deformation velocity at the previous RK-substep. Indeed, we estimated the effective incidence along the blades from the projection on each airfoil plane of the local relative flow velocity $\boldsymbol{U_{rel}}$, defined as:

$$\boldsymbol{U_{rel}} = \boldsymbol{U} - \boldsymbol{\Omega}\times\boldsymbol{R_{OP}} - \boldsymbol{v} \tag{14}$$

where $\boldsymbol{U}$ is the filtered velocity sampled at the position of the actuator line and $\boldsymbol{v} = \dot{\boldsymbol{d}}$ is the deformation velocity of the structure at that position. Finally, we obtained:

$$\alpha = \text{atan}\left(\frac{\boldsymbol{U_{rel}} \cdot \boldsymbol{E}_2}{-\boldsymbol{U_{rel}} \cdot \boldsymbol{E}_3}\right) - \phi = \text{atan}\left[\frac{(\boldsymbol{U} - \boldsymbol{v}) \cdot \boldsymbol{E}_2}{\Omega r - (\boldsymbol{U} - \boldsymbol{v}) \cdot \boldsymbol{E}_3}\right] - \phi, \tag{15}$$

$$U_{rel} = \sqrt{(\boldsymbol{U_{rel}} \cdot \boldsymbol{E}_2)^2 + (\boldsymbol{U_{rel}} \cdot \boldsymbol{E}_3)^2} \tag{16}$$

where $\boldsymbol{E}_i$ are the versors of the right-handed rotating FoR, with $\boldsymbol{E}_2$ indicating the streamwise direction, $\boldsymbol{E}_1$ indicating the radial direction pointing outwards, and $\boldsymbol{E}_3$ indicating the positive azimuthal direction. Hence, $\boldsymbol{U} \cdot \boldsymbol{E}_2$ is the streamwise absolute velocity component, $\boldsymbol{U} \cdot \boldsymbol{E}_3$ is the azimuthal absolute velocity component, $v_2 = \boldsymbol{v} \cdot \boldsymbol{E}_2$ and $v_3 = \boldsymbol{v} \cdot \boldsymbol{E}_3$ are respectively the flapwise (out-of-plane) and edgewise (in-plane) deformation velocities.

SETUP OF THE SIMULATIONS

We carried out our simulations for the NREL 5 MW wind turbine (Jonkman et al., 2009), which has a rotor diameter of 126 m. Detailed structural and aerodynamical data of the turbine are available and, moreover, several studies using different approaches have already analysed its behaviour (Hsu and Bazilevs, 2012, Churchfield et al., 2012, Heinz, 2013, Meng et al., 2018). Turbulence and wind shear represent relevant sources of unsteadiness for the structural dynamics, and can thus amplify the role of the structure in the aeroelastic interaction. Thus, we imposed a turbulent inflow with a mean power-law velocity profile, simulating a neutral Atmospheric Boundary Layer (ABL) with a hub velocity of 10 m/s and a shear exponent of $1/7$.
We imposed no-slip condition at the lower wall with Van Driest damping functions (Van Driest, 1956) to correct the flow behaviour at the wall, periodic conditions at the lateral boundaries, slip condition at the top wall and a radiative boundary condition at the outlet.

A grid of $1296 \times 432 \times 432$ points, in the streamwise, wall-normal and spanwise fixed directions respectively, discretised the fluid computational domain of $9.0D \times 10.0D \times 2.88D$, thus providing a resolution of 150 points per diameter. We located the turbine's hub at $2.95D$ from the inlet. For the structural dynamics, we chose a number of modes $M = 15$, discretised by a number of structural nodes $N = 80$. All the simulations run for approximately 36 revolutions, for a Reynolds number of 7×10^7 and the optimal tip speed ratio $\lambda = 7.5$.

RESULTS

In this section, we will indicate with *ALM* results, those obtained with one-way coupled simulations in which only the fluid solver passed the aerodynamic forces to the structural solver, and with *ALM/IV* (Induced Vibrations) results, those obtained with the coupled simulations in which also the structural solver passed the structural deformation velocity to the fluid solver.

We report in fig.1 the time history of the power and thrust coefficients. The time-averaged ALM and ALM/IV results are almost equal and, in general, the estimations agree with the BEM prediction. The drops in the coefficients reflect the periodic passage of the blades in front of the tower, as reported also in Hsu and Bazilevs (2012), and underline the importance of considering the tower in the fluid domain. However, the introduction of the coupling procedure modified the time behaviour, especially in the instants of and immediately after the negative peaks, whose intensity is reduced. This suggests that the tower represents a major source of unsteadiness for the structural dynamics, and that, by means of our aeroelastic model, we can detect the effect of this unsteadiness on the instantaneous aerodynamic loading, especially in the last quarter

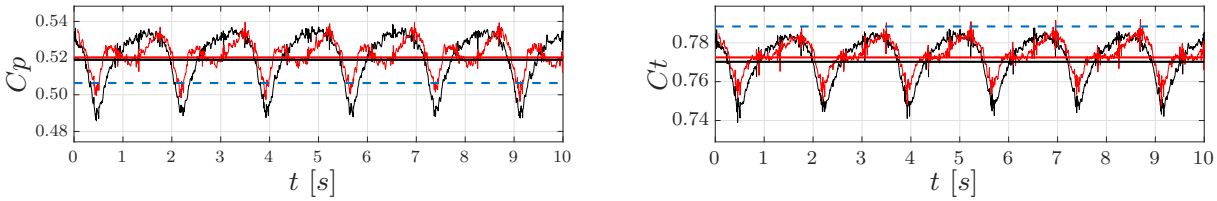

(a) Power coefficient. (b) Thrust coefficient.

Figure 1: **Time history of power and thrust coefficients for two revolutions. Respective time-averaged values are indicated with horizontal lines. ALM –, ALM/IV –, BEM – –.**

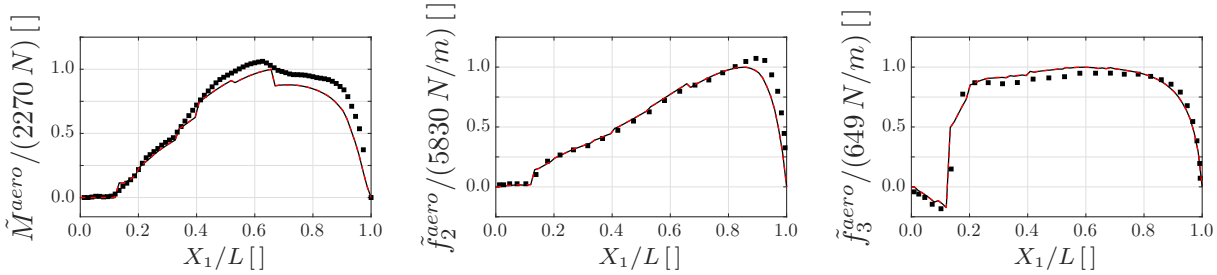

(a) (b) (c)

Figure 2: Time average along the blades of: a) aerodynamic moment, b) flapwise aerodynamic force, c) edgewise aerodynamic force. We normalised the aerodynamic forces to have a unitary maximum value for the in-house results. ALM –, ALM/IV – –, ■ HAWC2 (Heinz, 2013).

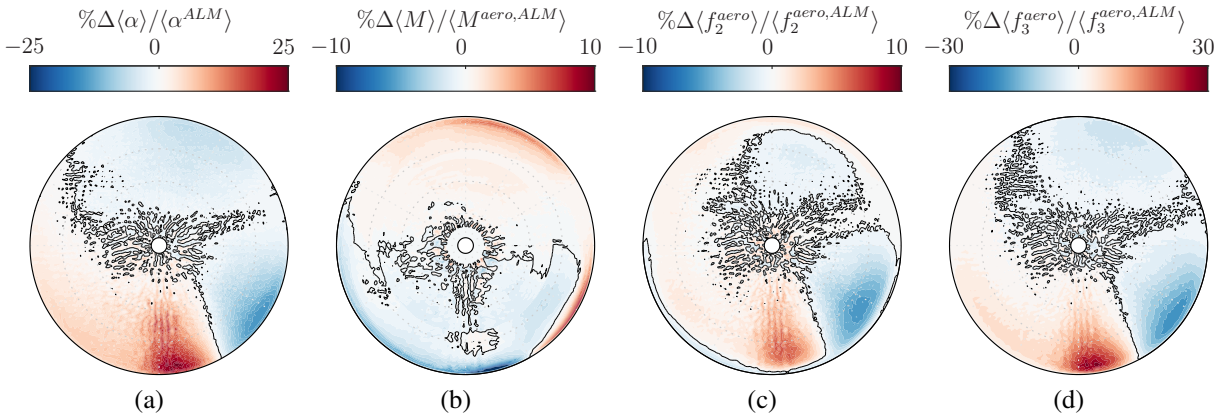

(a) (b) (c) (d)

Figure 3: Percentual difference between the ALM/IV and ALM cases with respect to the local values in the ALM case of the phase-averaged: a) incidence, b) aerodynamic moment, c) flapwise aerodynamic force component, d) edgewise aerodynamic force component.

of revolution of the blades. Figure 2 shows the time-averaged aerodynamic forces along the blades. The results obtained match well those of Heinz (2013) and confirm that this kind of coupling procedure does not influence the time-averaged behaviour. However, if we look at fig.3, where we show the percentual differences of the phase-averaged aerodynamic quantities between ALM and ALM/IV simulations with respect to the local values of the ALM case, we

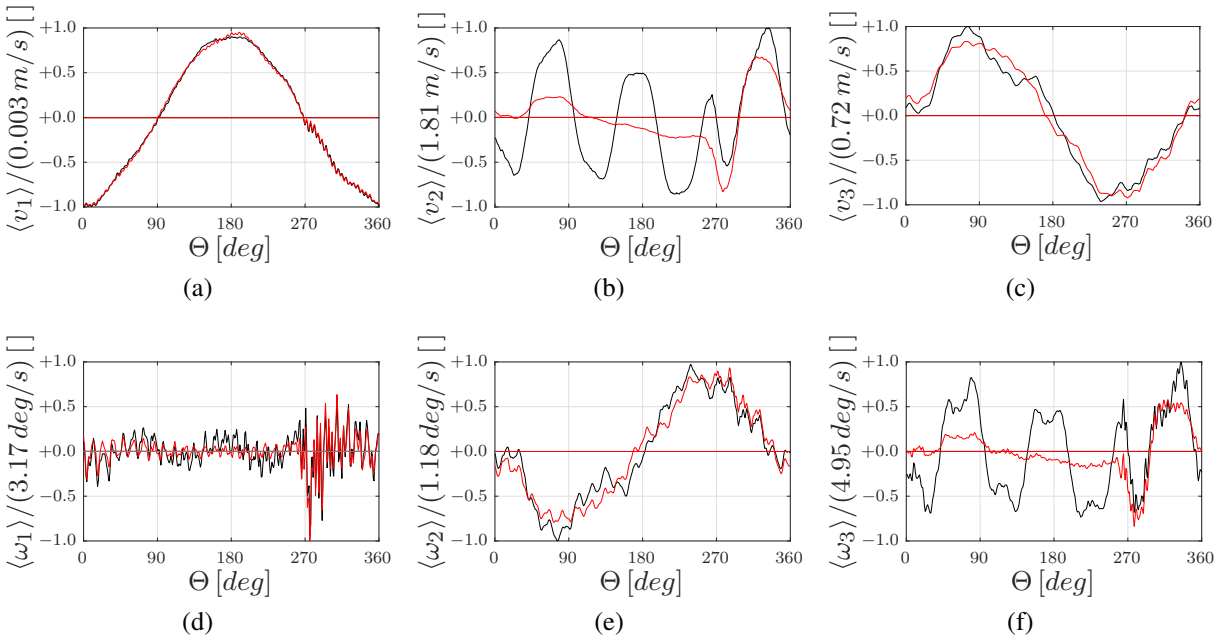

Figure 4: Phase-averaged deformation velocity at the blade tip. Unitary maximum normalisation. ALM –, ALM/IV –. DFs: a) axial translation, b) flapwise translation, c) edgewise translation, d) torsional rotation, e) edgewise rotation, f) flapwise rotation.

can observe a relevant variation in the fourth, and last, quadrant of rotation. An intense variation in the deformation velocity, especially in the flapwise component v_2, induces a sudden increase and then decrease of the local incidence. Indeed, because of its small value compared to the large rotational component Ωr, the edgewise velocity v_3 has only little influence on the angle of attack and the observed variations are mainly ascribable to the flapwise deformation.

Figure 4 reports the phase-averaged deformation velocities of the 6 structural DFs at the tip of the blade. The dominant component of the deformation velocity is the flapwise one $\langle v_2 \rangle$, which reaches peak values comparable with the flow velocity in the lowest part of the rotor.

From eq.15, a positive variation of the v_2 component reduces the incidence and viceversa, and in fact, the regions of positive $\langle v_2 \rangle$ in fig. 3 correspond to the regions of negative $\langle \alpha \rangle$ in fig.3.

We then reported in figure 5 the phase-averaged tip deformations. The mean values agree well with the results in other studies (Yu and Kwon, 2014). Gravity is the main force for the axial d_1 and in-plane d_2 and θ_2 structural dynamics, which are rather insensitive to the fluctuating aerodynamic forces, as reported also in Jeong et al. (2014). The introduction of the aeroelastic coupling has a strong effect on the out-of-plane bending d_2 and θ_3 and on the torsion θ_1, by inducing an important aerodynamic damping of the out-of-plane structural dynamics known in literature (Hansen, 2007). The high-frequency vibrations on the torsional Degree of Freedom (DF) are related to the sixth structural mode, the first torsional mode, at a frequency of $f_6 = 5.58\, Hz$. Moreover, the large impact of the passage of the blades in front of the tower is evident in the sudden jump of the deformations around the azimuthal position $\Theta = 270°$, which underlines the importance of a tower model also in the structural dynamics.

While the structural dynamics is deeply influenced by the aeroelastic coupling, the behaviour of the fluid quantities is relatively insensitive to the introduction of the deformation velocity in the expression of the relative velocity. In figure 6, we reported a general visualisation

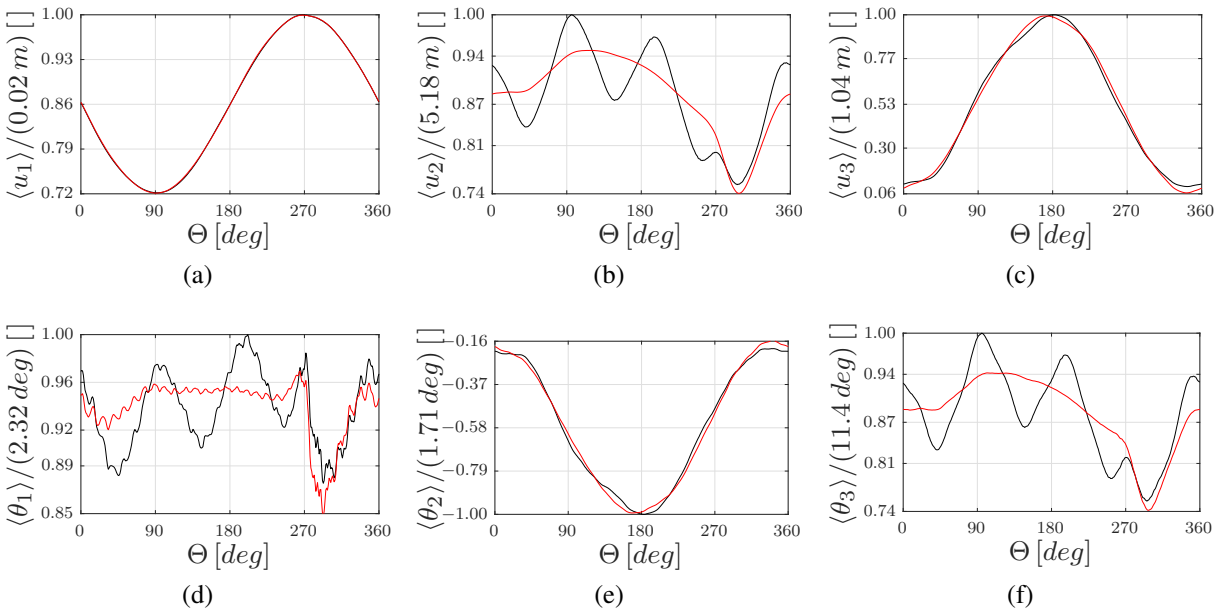

Figure 5: Phase-averaged displacement at the blade tip. Unitary maximum normalisation. ALM –, ALM/IV –. DFs: a) axial translation, b) flapwise translation, c) edgewise translation, d) torsional rotation, e) edgewise rotation, f) flapwise rotation.

of the wake for the ALM case, where we used the Q-criterion (Hunt et al., 1988) to identify the flow coherent structures. The tip vortices are dissipated by turbulence after approximately one diameter from the rotor, and their slope varies longitudinally because of the different convection velocity of the wake imposed by the sheared inflow. The root vortices instead are promptly suppressed by their interaction with the recirculating region behind the nacelle. We did not observe any significant difference between ALM and ALM/IV flow structures.

CONCLUSIONS

In this work, we presented a novel high-fidelity two-way coupling aeroelastic model for wind energy, which combines an LES fluid solver to a modal beam-like structural solver. A loose coupling leverages the ALM formulation that represents the rotor in the fluid domain, by utilising it as a fluid-structure interface to create an aeroelastic feedback. A blade element approach determines the local aerodynamic loads forcing instantaneously both structural and fluid dynamics, by defining the angle of attack as a function of the fluid velocity, provided by the fluid solver, and of the deformation velocity, provided by the structural solver.

For the NREL 5 MW turbine, we compared the cases with and without the described aeroelastic feedback mechanism. The results showed important variations in the instantaneous and phase-averaged behaviour of the structural and aerodynamic quantities, even if the time-averaged and fluid features were almost unchanged. In particular, we observed that the tower represents the main source of unsteadiness especially for the flapwise and the torsional motion. Moreover, the results confirmed the aerodynamic damping of the flapwise blade motion attested in other works. In the end, tip deformations in fig.5 suggest that the rotational deformation, torsion in particular, could play a significant role in the local incidence. Thus, future works will further develop the present model by progressively including the full elastic state.

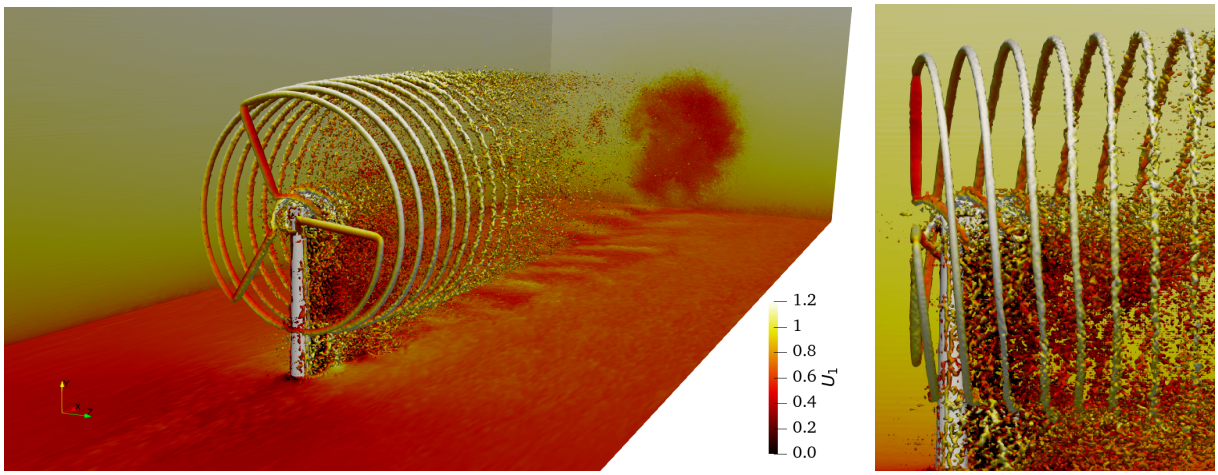

Figure 6: Instantaneous visualisation of the flow structures for the ALM case. A positive Q isosurface is shown and coloured, as the background slices, by the streamwise velocity U_1.

ACKNOWLEDGEMENTS

We acknowledge the Texas Advanced Computing Center (TACC) for providing the computational resources for this work. We thank F. Saltari and C. Santoni for the helpful discussion.

REFERENCES

Chung, J. and Hulbert, G. (1993), 'A time integration algorithm for structural dynamics with improved numerical dissipation: the generalized-α method', *J. Appl. Mech.* **60**(2), 371–375.

Churchfield, M. J., Lee, S., Michalakes, J. and Moriarty, P. J. (2012), 'A numerical study of the effects of atmospheric and wake turbulence on wind turbine dynamics', *J. Turbul.* **13**, N14.

Farhat, C. and Lesoinne, M. (1996), On the accuracy, stability, and performance of the solution of three-dimensional nonlinear transient aeroelastic problems by partitioned procedures, *in* '37th Structure, Structural Dynamics and Materials Conference', p. 1388.

Hansen, M. H. (2007), 'Aeroelastic instability problems for wind turbines', *Wind Energy* **10**(6), 551–577.

Heinz, J. C. (2013), Partitioned fluid-structure interaction for full rotor computations using CFD, PhD thesis, Technical Univ. of Denmark.

Hsu, M.-C. and Bazilevs, Y. (2012), 'Fluid–structure interaction modeling of wind turbines: simulating the full machine', *Comput. Mech.* **50**(6), 821–833.

Hunt, J., A, W. and Moin, A. (1988), Eddies, streams, and convergence zones in turbulent flows, *in* 'Center for Turbulence Research, Summer Program 1988', p. 198.

Jeong, M.-S., Cha, M.-C., Kim, S.-W., Lee, I. and Kim, T. (2014), 'Effects of torsional degree of freedom, geometric nonlinearity, and gravity on aeroelastic behavior of large-scale horizontal axis wind turbine blades under varying wind speed conditions', *J. Renew. Sustain. Ener.* **6**(2), 023126.

Jonkman, J., Butterfield, S., Musial, W. and Scott, G. (2009), Definition of a 5-mw reference wind turbine for offshore system development, Technical report, NREL.

Jonkman, J. M. and Buhl Jr, M. L. (2005), Fast user's guide, Technical report, NREL.

Komusanac, I., Fraile, D. and Brindley, G. (2019), Wind energy in europe in 2018, Technical report, EWEA.

Laks, J. H., Pao, L. Y. and Wright, A. D. (2009), Control of wind turbines: Past, present, and future, *in* '2009 american control conference', IEEE, pp. 2096–2103.

Larsen, T. J. and Hansen, A. M. (2007), How 2 hawc2, the user's manual, Technical report, Risø National Laboratory, Technical Univ. of Denmark.

Meng, H., Lien, F.-S. and Li, L. (2018), 'Elastic actuator line modelling for wake-induced fatigue analysis of horizontal axis wind turbine blade', *Renew. Energy* **116**, 423–437.

Orlandi, P. (2012), *Fluid flow phenomena: a numerical toolkit*, Vol. 55, Springer Science & Business Media (Saint Martin d'Heres Cedex, FRA).

Orlandi, P. and Leonardi, S. (2006), 'Dns of turbulent channel flows with two-and three-dimensional roughness', *J Turbul* (7), N73.

Reschke, C. (2005), Flight loads analysis with inertially coupled equations of motion, *in* 'AIAA Atmospheric Flight Mechanics Conference and Exhibit', p. 6026.

Saltari, F., Riso, C., Matteis, G. D. and Mastroddi, F. (2017), 'Finite-element-based modeling for flight dynamics and aeroelasticity of flexible aircraft', *J. Aircr.* **54**(6), 2350–2366.

Santoni, C., Carrasquillo, K., Arenas-Navarro, I. and Leonardi, S. (2017), 'Effect of tower and nacelle on the flow past a wind turbine', *Wind Energy* **20**(12), 1927–1939.

Shen, W. Z., Sørensen, J. N. and Mikkelsen, R. (2005), 'Tip loss correction for actuator/navier–stokes computations', *J. Sol. Energy Eng.* **127**(2), 209–213.

Simms, D., Schreck, S., Hand, M. and Fingersh, L. J. (2001), Nrel unsteady aerodynamics experiment in the nasa-ames wind tunnel: a comparison of predictions to measurements, Technical report, NREL.

Sorensen, J. N. and Shen, W. Z. (2002), 'Numerical modeling of wind turbine wakes', *J. Fluids Eng.* **124**(2), 393–399.

Troldborg, N., Sørensen, J. and Mikkelsen, R. (2009), Actuator line modeling of wind turbine wakes, PhD thesis, Technical Univ. of Denmark.

Van Driest, E. R. (1956), 'On turbulent flow near a wall', *J. Aeronaut. Sciences* **23**, 1007–1011.

Van Kuik, G., Peinke, J. et al. (2016), 'Long-term research challenges in wind energy–a research agenda by the european academy of wind energy', *Wind Energy Sci.* **1**(1), 1–39.

Yu, D. O. and Kwon, O. J. (2014), 'Predicting wind turbine blade loads and aeroelastic response using a coupled cfd–csd method', *Renew. Energy* **70**, 184–196.